Polymer Degradation and Stability 203 (2022) 110044

Contents lists available at ScienceDirect

Polymer Degradation and Stability

journal homepage: www.journals.elsevier.com/polymer-degradation-and-stability

Induced damage during STEM-EELS analyses on acrylic-based materials for Stereolithography

L.M. Valencia [a,*], M. de la Mata [a,*], M. Herrera [a], F.J. Delgado [a], J. Hernández-Saz [b], S.I. Molina [a]

[a] Departamento de Ciencia de los Materiales, I. M. y Q. I., IMEYMAT, Facultad de Ciencias, Universidad de Cádiz, Campus Río San Pedro, s/n, Puerto Real, Cádiz 11510, Spain
[b] Departamento de Ingeniería y Ciencia de los Materiales y del Transporte, Universidad de Sevilla, Avda. Camino de los Descubrimientos s/n., Sevilla 41092, Spain

ARTICLE INFO

Keywords:
STEM-EELS
Acrylic resin
Electron-beam damage
Degradation mechanism
Radiolysis
Knock-on

ABSTRACT

(Scanning) transmission electron microscopy, (S)TEM, offers a powerful characterization tool based on electron-matter interactions, highly valuable in materials science. However, the possible electron beam induced damage during (S)TEM measurements hinders the analysis of soft materials, such as acrylic resins. Importantly, acrylic resins offer an appealing playground for the development of novel composites with customized properties and convenient processing capabilities for 3D-printing technologies, including Stereolithography (SLA). There are several factors preventing the optimal performance of TEM measurements applied to acrylic resins, among which we focus on the quality of the analyzed specimen (i.e., compromise between thickness and robustness, to achieve electron transparency while keeping the material integrity), particularly challenging when working with soft materials; the electrostatic charging/discharging effects, resulting in sample drift and related noise/artefacts; and the radiolysis and knock-on electron-induced damage, which directly degrade the material under study. We explore and compare different methodologies to obtain resin specimens suitable for (S)TEM analysis, employed for the subsequent study of the electron–beam damage induced during STEM-EELS measurements. Furthermore, we propose likely underlying mechanisms explaining the acrylic resin degradation based on the different EELS monitored signals. On one hand, we assess the evolution of the carbon and oxygen content, as well as the material thinning as a function of the accumulated electron dose. On the other hand, we extract meaningful information from the spectral shape of carbon and oxygen K-edges upon increasing electron doses, unraveling likely degradation pathways. The earned understanding on the electron-beam induced damage and the determination of critical doses provide a useful framework for the implementation of (S)TEM techniques as useful tools to help in the smart engineering of acrylic-based composites for SLA.

1. Introduction

Understanding the functional properties of novel materials requires from their characterization at the highest resolution attainable, particularly dealing with nanocomposite materials. (Scanning) Transmission electron microscopy, (S)TEM, techniques outstand within this context, providing sub-nanometer structural and chemical information [1–4]. The implementation of (S)TEM techniques to nanocomposite materials [5–11] allows, for instance, mapping the distribution and morphology of nanoaditives or nanodomains, addressing possible phase segregation and interdiffusion phenomena with sub-nanometer resolution, etc., which are consequence of the synthesis/processing procedures while dictate their properties. Thus, (S)TEM techniques provide useful tools for the material engineering, by correlating the results to the material performance, and for the design and optimization of the synthesis/processing routes, by the correlation to the experimental parameters used.

In addition to the variety of imaging techniques available under (S)TEM conditions, different electron-matter signals can be monitored implementing spectroscopic techniques to address composition information and opto-electronic properties. In particular, electron energy loss spectroscopy (EELS) is an appealing characterization technique that

Abbreviations: STEM, Scanning Transmission Electron Microscopy; EELS, Electron Energy Loss Spectroscopy; LOM, Light Optical Microscopy; MLLS (fit), Multiple Linear Least Square (fit); FIB, Focused Ion Beam; UM, Ultramicrotomy; Dc, Critical Dose; SLA, Stereolithography.

* Corresponding authors.
E-mail addresses: luisamaria.valencia@uca.es (L.M. Valencia), maria.delamata@uca.es (M. de la Mata).

https://doi.org/10.1016/j.polymdegradstab.2022.110044
Received 16 June 2022; Received in revised form 23 June 2022; Accepted 25 June 2022
Available online 5 July 2022

measures the kinetic energy lost by the impinging electrons due to inelastic scattering while crossing the material specimen. The collection of these inelastically scattered electrons spread apart attending to their energy lost results into EEL spectra [12]. The region between 0 and 50 eV, known as low-loss region, corresponds to the excitation of the outer electron shells of the atoms constituting the material, whose energy states lie within the first tens of eV below the Fermi level. Consequently, low-loss EELS accesses the opto-electronic properties of the materials, including interband transitions, bandgap measurements, plasmonic characterizations, etc., highly valuable for the characterization of photonic materials. The unique simultaneous spatial and spectral resolution rendered by the technique, achieving up to a few meV if using monochromated electron probes, find countless applications in nanoscience. For instance, it is widely employed for the study of localize surface plasmon resonances (LSPR) and other nanosystems optically or electronically active, such as nanoantennas or different confined systems (2D materials, for example). Notably, the current state-of-the-art of the technique accesses the IR spectral range, becoming suitable for the study of phonon-related phenomena (only at aberration-corrected dedicated STEM instruments equipped with highly stable monochromators [13]). Additionally, the multiple scattering events related to the actual sample thickness are also reflected at low-loss spectra, rendering information on thickness variations, gradients or fluctuations. The core-loss region (above 50 eV) represents the inner-core electronic structure of sample constituents, with characteristic energy losses for each element. Thus, while core-loss spectra are suitable for the chemical characterization of the material, including the analysis of bonding and coordination states, low-loss spectra contains higher frequency signatures on the atomic electronic states which allow, for instance, assessing the material thickness based on the analysis of multiple plasmon excitations [14–16].

Polymeric systems offer a rich playground for the development of new materials, suitable for 3D-printing approaches, such as Stereolithography (SLA) technique, which facilitates the production of complex three dimensional objects using computer-aided designs with countless application fields [17]. The basic principle of the process is to solidify a photocurable resin from a mixture of monomers and oligomers along with a photoinitiator triggering the cross-linking reaction (i.e., radical mechanism) and reactive diluents, by using a UV laser source to build up the entire object layer-by-layer. Acrylic resins are suitable candidates for SLA since they allow UV assisted cross-polimerization. Consequently, there is a growing interest driving the development of acrylic-based composites with tailored properties, requiring from deep material characterizations. The smart engineering of nanocomposites with customized properties (oriented for their processing and final performance) relies on establishing the proper connections to their composition and microstructure, attainable by (S)TEM-EELS. Spectral fingerprints at both, the low-loss and the core-loss regions, allow the distinction among chemical phases based on the differentiated chemical bonding state of carbon K-edge within epoxy/carbon fiber composites [18]. The measurements can be oriented, for intance, to estimate the loading fraction of composites, as reported Liu et al. [19] for GO/epoxy and GNP/epoxy composites, including studies on the interphase region between the nanofillers and the matrix. Furthermore, spatially resolved EELS combined with (S)TEM imaging have been employed as an effective way to study nanoscale morphologies of different polymer systems [20,21]. In particular, the energy-loss near-edge structure (ELNES) within the core-loss region relates to the bonding and coordination states of the atomic species present in the sample. Consequently, ELNES provides characteristic siganatures for every material, including polymers [16,22,23], useful for their late identification. Despite the numerous advantages rendered by EELS, its implementation to polymeric materials remains largely under-exploited. One of the major reasons is the high beam sensitivity of polymeric materials. Polymers, such as acrylic resins, are prone to damage under the electron beam resulting in the ease degradation during (S)TEM-EELS measurements, either by chain scission or cross-linking [24]. To this end, the development of (S)TEM approaches and methodologies for imaging irradiation-vulnerable materials is crucial. This does not preclude the use of (S)TEM-EELS as a characterization technique but rather requires full characterization of polymer spectra, including identification of loss peaks which may result from radiation damage to the polymer itself, and accurate knowledge of experimental parameters.

Importantly, the performance of (S)TEM analyses requires from clean and thin lamellae material specimens, ideally thinner than 100 nm, which entails a first challenge working with polymeric materials. (S)TEM samples must be electron transparent and thin enough to prevent multiple scattering events, in order to accurately examine their composition, morphology and nanostructure. Specimen preparation techniques must provide uniform large thin areas from the target material (unaltered) in a repeatable fashion. There are several well established (S)TEM specimen preparation methodologies, and choosing the most convenient one depending on the material characteristics is particularly important. Sequential mechanical polishing and ion milling is a common strategy applied to brittle and hard materials (i.e., ceramics, metals and alloys) where large areas and volumes of sample are necessary [25]. Focused ion beam (FIB) provides another (S)TEM specimen preparation technique, consisting on thining down the material by focalized gallium ion beams [26]. Another well-known approach, particularly used when dealing with polymer samples, is ultramicrotomy (UM), consisting on directly slicing electron-transparent sections of the material, about tens of nanometers to a micron thick [27]. Sharp knives, often made from diamond, tungsten carbide, or glass, are used to create a small crack in the sample, which propagates through the material to end up cutting a thin section [28].

The next challenge regards minimizing the damage due to electron-specimen interactions during the (S)TEM experiments that result in significant degradation of the spatial resolution, and which ultimately limits the quality and the accuracy of the measurements. The intrinsic soft nature of polymers along with their poor electronic conductivity are intimately related with their low stability under electron irradiation. However, the exact mechanism promoting the material degradation is not fully understood yet, while it depends strongly on the exact experimental conditions and the material analyzed. There might be several processes contributing to the overall electron beam damage, including elastic and inelastic scattering, which lead to atomic displacement, knock-on damage, radiolysis, electrostatic charging and local heating, among others [29,30]. The principal beam damage processes likely to happen working with polymer samples are electrostatic charging, radiolysis and knock-on damage [31,32]. Electrostatic charging is induced by the ejection of secondary and Auger electrons into vacuum from electronically insulator materials, such as polymers, creating local charges [33]. Radiolysis occurs due to atomic ionization driven by inelastic scattering (i.e., electron energy transfer), and results in atomic displacements [29]. Polymers and resins are especially prone to radiolysis and their large inelastic scattering may lead to chemical changes, such as the breakage of chemical bonds and loss of atomic structure followed by ejection of atoms from the sample (mass loss) [34,35]. Knock-on damage is due to elastic scattering induced by the incident electron, promoting the displacement of the atoms from their lattice sites, thus, creating coupled atomic defects (i.e., simultaneous creation of an interstitial impurity and an atomic vacancy) [29,36].

Electron beam damage can be addressed by monitoring the changes at a measured signal upon electron irradiation, for example the intensity fading of Bragg reflections at electron diffraction patterns [37]. The available bibliography on the topic suggests that the damage depends on many factors, such as the dose rate (electron current density), the accumulated dose (electrons per unit area), or the accelerating voltage [24,32]. The critical dose (D_c) to produce meaningful electron damage is usually defined as the exponential decay of the signal intensity (I):

$$I = I_0/e \quad (1)$$

being I_0 the initial signal intensity of the unirradiated material.

Addresing the material response upon electron irradiation during (S)TEM experiments provide safe experimental conditions (i.e., preventing major induced signal modifications). Thus, the topic has been extensively examined covering a variety of polymer related materials (nanocomposites and polymer blends to be used in organic photovoltaics (OPVs) [35,38,39], organic electronics [40,41] and polymer electrolyte membranes (PEMs) [21,22]) with diverse results [31,35,40,42–44]. However, this type of analysis has never been focused on SLA acrylic resins before, which opens up to the characterization of novel nanocomposites for an enabling technology of Industry 4.0.

We study the electron-induced damage in a commonly employed SLA acrylic resin by means of STEM-EELS, including the evaluation of different sample preparation methodologies to obtain suitable (S)TEM specimens, and the effect of the accumulated electron doses during the analysis. More specifically, the quality of polished and milled (from now on referred to as *mechanical thinning*), FIB and UM specimens from an acrylic resin are compared highlighting their respective limitations and advantages. The electrostatic charging effect is evaluated for Cu and Au supporting grids, and some amorphous and conductive coatings (such as amorphous carbon and graphene films). We analyze the electron-beam damage mechanism by monitoring the variations on the C and O K-edges along with the thickness reduction upon electron dose accumulation during EELS experiments. Furthermore, we address the spectral evolution of the EELS C and O K-edges as a function of the accumulated dose, unraveling chemical variations during the beam exposure likely due to the scission and cross-linking of the resin.

2. Materials and methods

2.1. Materials

Clear photopolymer standard UV curable resin (a mixture of proprietary acrylic monomers (30–40 wt%), trimethylolpropane triacrylated (20–30 wt%) and urethane acrylate oligomers (30–40 wt%), and phenylbis (2,4,6-trimethyl benzoyl)-phosphine oxide as photoinitiator (0–5 wt%)) was purchased from XYZprinting, Inc.

2.2. Sample preparation

Solid samples have been printed by SLA with an equipment Nobel 1.0, XYZprinting, Inc., using a 405 nm laser with an output power of 100 mW and a spot size achieving an XY resolution of 300 μm.

TEM electron-transparent specimens from solid samples were obtained using three different methods:

- Mechanical thinning by polishing the materials down to about 1 μm thickness, using a Target Surfacing System Leica EM TXP and diamond lapping films with grain sizes smaller than 1 μm; followed by Ar^+ ion milling at 3 keV during 2 h using Gatan precision ion polishing system (PIPS).
- Focus Ion Beam (FIB) using a Scios 2 DualBeam (Thermo Scientific) combined with FIB-scanning electron microscope (FIB-SEM). Prior to thinning, the area of interest is coated by a protective Pt layer deposited at 30 kV and 0.1 nA. Afterwards, the lamella was extracted and thinned by Ga ions at 30 kV and decreasing the current between 0.1 and 0.03 nA. At the final stage, the sample was very thin, so further milling would likely result in the sample being broken. Finally, cleaning was done at 5 kV leaving the lamella with the desired thickness.
- Ultramicrotomy: thin films of about 70 nm were obtained using a Leica EM UC7 ultramicrotome equipped with a diamond knife. After cutting, the cross sections floating on water were directly collected using 300 mesh Cu grids. 300 mesh Cu grid, 300 mesh Au grid, 2000 mesh Cu grid with a single layer of graphene and ultrathin (~2 nm) amorphous carbon film and holey carbon film, both supported on Cu grids have been used to analyze the electrical charging effect.

2.3. Characterization

Optical measurements have been carried out in an inverted metallurgical microscope Eclipse MA100 from Nikon.

EELS measurements were performed by using a 60–300 kV Titan Cube FEI transmission electron microscope provided with a X-FEG Schottky electron gun and equipped with a Cs-probe corrector and a Gatan Dual EELS Spectrometer, operated at 200 kV. Dual (low-loss and core-loss) time series EELS spectra were acquired using an energy dispersion of 0.25 eV/ch at currents of 50, 70 and 85 pA, by scanning fixed areas of 24 × 24 px^2 (pixel size of $8.3{\cdot}10^{-3}$ $Å^{-1}$), with exposure times of 0.0005 s up to 0.1 s per pixel. The convergence and collection angles employed were 21.4 and 13.3 mrad, respectively, and dose rates of 20, 40, 50 and 80 e/$Å^2$s were used.

2.4. Data analysis

Data have been proccessed using Gatan Digital Micrograph software. Dual time-series spectrum images were aligned with the zero-loss peak. Thickness maps were computed by using the relative log-ratio algorithm, providing the thickness over inelastic mean free path (λ) ratio, t/λ, of the analyzed area. The theoretical inelastic mean free path was calculated by means of Iakoubovskii's equation [45,46] implemented at the *mean free path estimator* tool available for Gatan Digital Micrograph software package. The resulting λ for the acrylic resin is 180 nm. Core-loss spectra have been denoised by principal component analysis (PCA) before multiple linear least square (MLLS) fitting. Reference spectra for the MLLS fitting were set as the first and last spectra extracted from the experimental series stack, being reference for undamaged material and the material before breaking, respectively. Carbon K-edge (280–305 eV) and oxygen K-edge (520–560 eV) have been extracted and compared separately.

3. Results and discussion

3.1. Optimization of acrylic resin TEM specimens

We have compared the ability of three different TEM specimen preparation methods to produce good quality acrylic resin specimens, namely mechanical thinning, FIB and UM. The quality of the different specimens has been evaluated by light optical microscopy (LOM), TEM imaging and low-loss EELS measurements, summarized in Fig. 1. LOM and TEM imaging address the lateral dimensions of the specimens as well as possible wrapping/folding and related features, while low-loss EELS analysis provide the relative thickness of the samples intended for (S)TEM studies.

The mechanically thinned specimen offers a large area for the analysis, about $2{\cdot}10^6$ $μm^2$ (Fig. 1a). However, the obtained specimens are very thick, around 1–5 μm, with strong thickness variations. The holes drilled during the ion milling process provide thinner areas, few nanometers wide, with thicknesses below 1 μm (light blue circle in Fig. 1a and b) that allow collecting EELS spectra to estimate the thickness (t) over inelastic mean-free path (λ, how far an electron on average travels through a solid before losing energy) ratio (Fig. 1c). The thickness maps evidence that the small area of analysis provided is too rough and thick, with a mean t/λ of 2.2 ± 1.3 (see Fig. S1 at the Supporting Information for more details). Thus, despite of being a well-established methodology, widely employed for crystalline samples [25], mechanical thinning does not work properly facing acrylic resins, as it results in thick specimens with remarkable thickness variations, hardly useful for TEM analysis (see Table 1). More LOM and TEM images of further examples at different conditions can be found in Fig. S2 (Supporting Information).

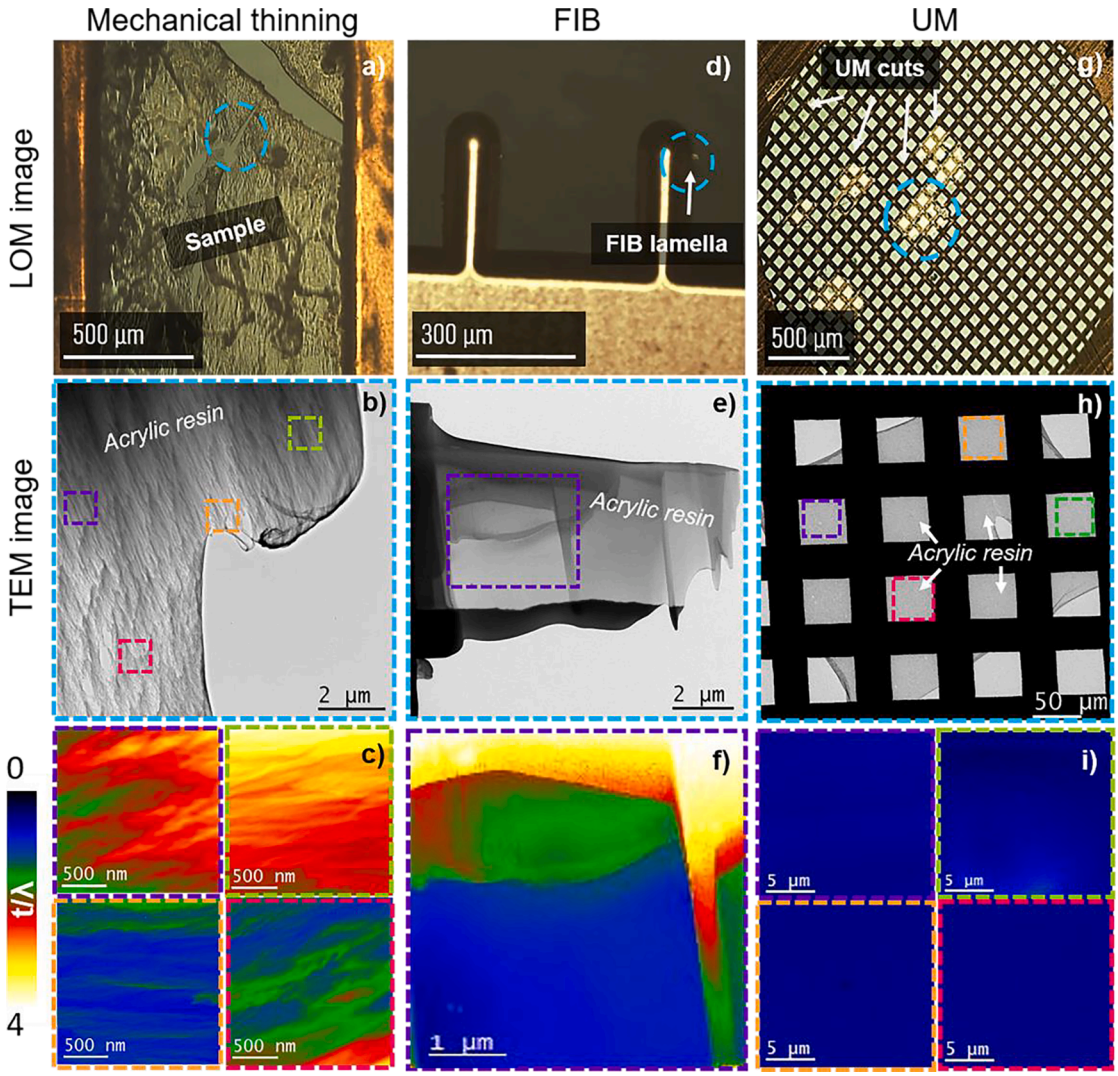

Fig. 1. LOM images (top row), TEM images (middle row) and low-loss EELS thickness maps (bottom row) of the TEM acrylic specimens prepared by mechanical thinning (a–c), FIB (b–h) and UM (g–i). The TEM images correspond to the areas marked with a light blue circle in the LOM images; and the thickness maps correspond to the squared areas in panels (b), (e) and (h).

Table 1
Areas, t/λ and experimental thicknesses of Mechanical thinning, FIB and UM preparation methods. (◆ *n*: number of UM cuts).

	Specimen Area (μm^2)	Relative thickness (t/λ)	Experimental thickness (nm)
Mechanical Thinning	10^6	2.1 ± 1.3	396 ± 234
FIB	10^2	0.7 ± 0.2	126 ± 36
UM	$(10^5)_n$◆	0.28 ± 0.04	50 ± 7

Fig. 1d and e show LOM and TEM images, respectively, from the FIB lamella. The light blue circle in Fig. 1d points the region displayed in Fig. 1e, corresponding to the studied area by TEM. FIB provides surface areas smaller than mechanical thinning (usually, around 20 × 10 μm^2, see Table 1), while renders better control over the specimen thickness, with additional benefits. In order to prevent wrapping/folding of the lamellae, an intended thickness gradient was intentionally designed leading to thicker (t/λ = 2.1 ± 0.3) and thinner (t/λ = 0.7 ± 0.2) areas at opposite sides of the sample (Fig. 1f). Fig. S4 (Supporting Information) illustrates further examples of other polymers and blends prepared by FIB, evidencing the ultimate role of the material on the lamellae thickness and quality.

Fig. 1g–i shows the LOM image, TEM image and thickness map, respectively, for the acrylic resin specimen obtained by UM. In addition to the large lateral size of each UM cut ($9 \cdot 10^4$ μm^2 in this specific case), one remarkable advantage of UM is the feasibility of collecting several slices at one single grid, thus, offering large electron-transparent areas faster than those obtained by FIB or mechanical thinning. The thinnest sections achievable by using glass knives are about 100 nm (see Fig. S5, Supporting Information), however, these sections are strongly irregular. Thinner slices are possible by using diamond instead of glass knives, reaching homogeneous sections as thin as ~30 nm. To properly analyze the quality of these samples, specimens with intended thicknesses of 30, 50, 70 and 90 nm have been prepared, resulting in experimental t/λ values of 0.14 ± 0.03, 0.20 ± 0.05, 0.28 ± 0.04 and 0.30 ± 0.08, respectively (see Supporting Information, Fig. S6a). The acrylic resin theoretical inelastic mean free path (λ) calculated following Iakoubovskii's equation results in 180 nm; consequently, the estimated experimental thickness values are 25 ± 6, 36 ± 10, 50 ± 7 and 54 ± 14 nm, respectively (see Supporting Information, Fig. S6b). Fig. 1i shows the thickness maps of the squared areas in Fig. 1h (from a 70 nm intended thick sample cut by UM), evidencing the above-mentioned thickness homogeneity of the UM slices (t/λ = 0.28 ± 0.04 and, consequently, 50 ± 7 nm) (see Fig. S7, Supporting Information). It should be mentioned that thick samples (≥ 100 nm) may be convenient

or even required for certain analyses, such as electron tomography. However, for EELS analyses, the sample should be as thin as possible to reduce detrimental multiple scattering effects, while too thin samples do not have enough structural consistency and can suffer shrinkage with the electron beam. In our case, samples thinner than 50 nm easily break under the electron beam of the microscope. Therefore, in the following, we proceed with the study of the electron-beam damage induced on the SLA acrylic resin by analyzing UM specimens 50 nm thick ($t/\lambda \approx 0.28 \pm 0.04$).

3.2. Evaluation of the electrostatic charging effect

Once the most suitable preparation method to obtain electron-transparent acrylic resin specimens is established, we study the samples under STEM conditions to address the electron-induced beam damage during the measurements. The irradiation of any specimen by high-energy electrons produces secondary electrons that escape from its surface. As a result, insulator materials, such as acrylic resins, would become positively charged, causing electron beam-induced movement that hinders STEM analysis. Different strategies have been proposed to minimize this mechanical movement when working with sensitive materials, mostly based on using electrically conductor supporting grids with or without films or coatings. In this context, we have assessed the effect of two different metal grids, Au and Cu, on our specific case of study dealing with acrylic resins. Russo and Passmore [47] have reported the advantageous use of Au supports for electron cryo-microscopy (cryo-EM) applied to biological specimens, which reduces the radiation-induced movement and image blurring due to the increased conductivity of these substrates compared to other less conductive, such as carbon substrates. In our case, the use of Au grids resulted in a larger image drift than that for Cu grids at high magnifications, due to the higher conductivity of Cu. Otherwise, the use of amorphous carbon [48] or another conductive layer [49,50] suspended across the metal grid may minimize or eliminate charging effects in (cryo-)TEM analyses of sensitive materials. In our case, we have noticed that using Cu grids coupled with carbon coatings of graphene single layer, holey carbon film or carbon sputtering successfully minimized the sample movement and slightly reduced the discharging effects compared to the naked Cu grid, allowing the acquisition of high magnification images. Nonetheless, using carbon coatings might interfere with our analysis as the acrylic resin is an amorphous material mainly composed by carbon. Therefore, in order to avoid external artefacts, we have chosen to directly deposit the UM cuts on naked Cu grids for the (S)TEM analysis.

3.3. Study of mass loss phenomena

Electron irradiation during (S)TEM analyses of soft materials may result in material sputtering until breakage. The mass loss is a consequence of the polymer chain scission trigged by bond breakage at the external surfaces of the sample [51], where elastic and inelastic scattering may play different roles [17,24]. While elastic and inelastic scattering occur in all materials, the inelastic contribution will depend on the dielectric properties of the sample [52]. Thus, the degradation mechanism inducing the mass loss is not universal and it can involve one or several processes (i.e., radiolysis and knock-on damage).

We have analyzed the mass loss effect taking place while the electron beam impinges into the acrylic resin in order to shed light into the underlying degradation mechanism. We have acquired sequential EELS spectra over the same area, monitoring the related signals as a function of the exposure time, hence, as a function of the accumulated dose for fixed dose rates. Low-loss spectra provide information on the thickness variation of the sample during electron irradiation while acquiring the data. Fig. 2a shows the evolution of the sample thickness (t/λ) with the accumulated electron dose for a UM specimen with thickness 0.24 using 20 e/Å^{2}s. The critical doses (defined as the accumulated electron dose at which the thickness decreases to 1/e (~37%)) obtained for acrylic resin samples with initial relative thicknesses between 0.1 and 0.3 is on the order of 10^3 e/Å^2, while thicker samples (above 0.3 t/λ) reach critical doses five times larger ($5{\cdot}10^3$ e/Å^2) (specimens with a thickness bellow 0.1 have not been prepared, see Section 3.1). It must be noted that the radiation sensitivity for a certain material may depend on the initial thickness of the specimen [53], increasing the critical dose for thicker samples, in agreement with our results. Herein we focus on thicknesses < 0.3, since these values predominate in our samples. Regardless of the initital specimen thickness, the thinning with the accumulated dose shows two differentiated regions (Fig. 2a), starting with a fast thickness drop followed by a slower thinning.

The observed thickness evolution as a function of the accumulated dose can be modelled by considering two subsequent processes. At low accumulated doses the thickness decays exponentially in agreement with a first-order process (exponential fall-off), while the material thinning is linearly proportional to the accumulated dose for high accumulated doses. Accounting for this observation, we have divided the experimental curve into two separated parts, fitted independently. For electron doses below 10^2 e/Å^2, the mass loss nearly follows a first-order process with an exponential dose dependence, in agreement with *Egerton* [32]:

$$t \approx t_0 \cdot \exp(-D / D_c) \quad (2)$$

where t_0 is the initial thickness of the sample, t is the thickness at a given accumulated dose D and D_c is the critical dose. Importantly, radiolysis

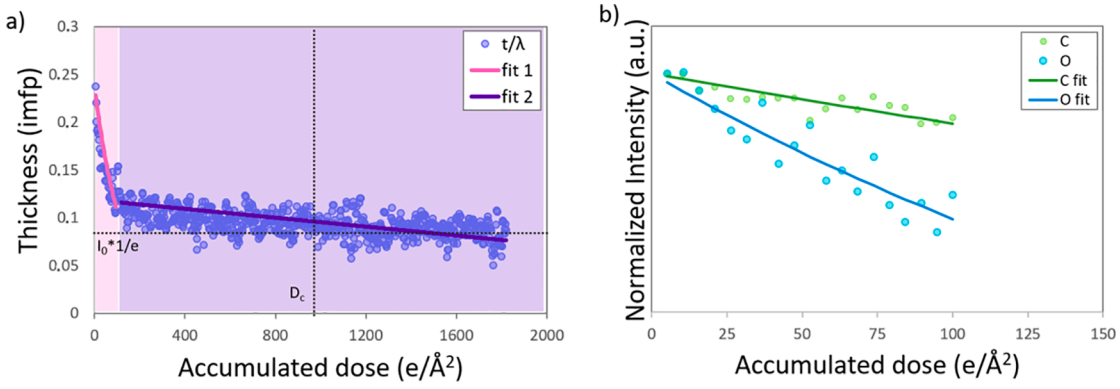

Fig. 2. (a) Thickness variation of an acrylic resin specimen during electron beam exposure at 20 e/Å^{2}s (blue), including the data fitting to the radiolysis equation (Eq. (1)) for low accumulated doses (pink), and to the knock-on equation (Eq. (2)) for high accumulated doses (purple); (b) C (green) and O (cyan) K-edge normalized intensities vs. accumulated dose and their fit to the radiolysis equation (Eq. (3)).

degradation follows a first-order expression with an exponential dose dependence, suggesting the chief role of radiolysis on the observed thickness reduction before reaching a certain accumulated dose threshold (i.e., 10^2 e/Å^2).

From 10^2 e/Å^{2}s on, the mass loss is directly related to the accumulated dose, in agreement with a zero-order process [32], following the equation:

$$t \approx t_k - t_k \cdot \sigma_d \cdot D \quad (3)$$

where t_k is the thickness after the exponential loss (i.e., thickness reached for 10^2 e/Å^2) and σ_d is the displacement cross section per atom (q/D_c, being q the electron charge and D_c the critical dose). As the material sputtering is basically a zero-order proccess with the electron dose, knock-on damage would explain the mass loss observed for high accumulated doses (i.e., higher than 10^2 e/Å^2).

Fig. 2a displays both fits: Fit 1 labels the exponential data fit as expected for radiolysis damage (pink plotted), and fit 2 is the linear regression indicative of knock-on damage (purple plotted). The resulting equations for the acrylic specimen (fit 1 and fit 2, respectively) (initial thickness $0.3 > t/\lambda > 0.1$), are

$$t \approx t_0 \cdot \exp\left(-D / 1 \cdot 10^3\right) \quad (4)$$

and

$$t \approx t_k - 5 \cdot 10^{-5} \cdot D \quad (5)$$

(see Supporting Information, Section 2 for more information). Therefore, we suggest that the acrylic resin thinning upon STEM-EELS irradiation attends to two subsequent processes: initially, radiolysis phenomena reduces the thickness up to approximately half of the initial value, followed by knock-on phenomena until breakage. While for most organic materials the main reported damage mechanism is radiolysis [32,34,54,55], other studies reported the material degradation following inelastic and elastic dominated scattering proccesses (associated to radiolysis and knock-on damage, respectively) taking place sequentially, similar to our observations. This behavior has been addressed on epoxy resins by analyzing the section shrinkage at dose rates of 1–70 e/Å^{2}s, resulting in a first-order decay for low accumulated doses, and a linear dependence for high accumulated doses [56]. Guo et al. [34] have also reported the same tendency for rr-P3HT (regioregular poly(3-hexylthiophene-2,5-diyl)), where the integrated intensity of the low-loss EELS signal initially shows an exponential decay with the accumulated dose, switching to a linear behavior for a certain accumulated dose. Thus, for organic specimens, such as acrylic resins, radiolysis is the predominant damage mechanism; however, if the energy of incident electrons is high enough to overcome the threshold energy of atomic sputtering (< 100 KeV for carbon), knock-on displacement may become noticeable [52,57,58]. Another parameter commonly employed to quantify the material damage is the cross section (σ_d), which is inversely proportional to the critical doses [57]. Since knock-on cross-sections are smaller than those of radiolysis, higher critical doses are expected for knock-on displacement [32], in agreement with our results (see Section 2, Supporting Information).

Core-loss EELS spectra were recorded simultaneously to the low-loss data, rendering information on the kinetics of carbon and oxygen losses. Fig. 2b shows both, carbon and oxygen K-edge normalized intensities (after standard background subtraction), plotted as a function of the accumulated dose, along with their fitting to equation:

$$I \approx I_0 \exp(-D / D_c) \quad (6)$$

being I and I_0 the carbon(oxygen) K-edge intensity for a given accumulated dose, D, and the initial intensity, respectively. Thus, there is an exponential decay of both signals for low accumulated doses, similar to the overall mass thining above-demonstrated. Interestingly, both, carbon and oxygen losses are in agreement with a first-order process, each of them showing differentiated kinetics. The oxygen loss rate (light bue circles) is four times faster than the carbon one (i.e., calculated exponential indexes of -D/8·10^2 (± 3·10^2) and -D/2·10^2 (± 7·10^1) for carbon and oxygen, respectively). Both rates are estimated by fitting the carbon and oxygen data to Eq. (6). Due to the lower D_c of oxygen, the oxygen exponential decay is steeper than the carbon decay, pointing the easier oxygen loss under the electron beam irradiation. As we will see in the following sections, this is likely related to the loss of oxygen through carboxyl groups for accumulated doses below 2·10^2 e/Å^2. To deepen the study of the electron induced damage of acrylic resin during STEM-EELS measurementes, we take advantage of the chemical fingerprint provided by the EELS data.

3.4. Investigations on the scission and cross-linking phenomena during EELS irradiation

The mass loss process is often accompanied by a change in the chemical composition of the analized material due to the different binding energies of the atomic species conforming the sample [29,59]. The core-loss EELS fine structure contains information on the bonding and coordination states of the sample constituents, providing the fingerprints of the species within the particular material phase studied. Fig. 3a shows the carbon and oxygen EELS K-edges, recorded at different accumulated doses (upper inset). Dose-resolved series of spectra were collected from the acrylic resin by continuously irradiating the same area of the sample, and recording spectra at periodic time intervals until complete degradation (i.e., upon sample breakage). The changes in the shape of the edges upon irradiation are associated to the electron beam damage during the measurements. The carbon K-edge shows the typical shape of amorphous carbon, with a pre-peak at ~283 eV associated to π* transitions and a main peak from ~285 eV, related to C σ* states. Herein, the pre-peak and peak are labelled as π* and σ*, respectively. In the case of the acrylic resin, the presence of the pre-peak at ~283 eV is consistent with likely C 1s → π* transitions, while the main peak would contain further contributions from the carbonyl group (Fig. 3b) [23,59–61]. The oxygen K-edge signal, noiser and much less intense (since the oxygen content is lower, and probably due to its higher electron sensitivity), appears at around 529 eV.

Importantly, there is a clear change on the spectral shape with the accumulated electron dose (Fig. 3a and b), noticeable at both, carbon and oxygen K-edges for doses below 10^3 e/Å^2 (i.e., before reaching the calculated D_c). Whithin this regime, the oxygen K-edge intensity fades with increasing accumulated doses, reaching the detection limit already at 870 e/Å^2. For such an accumulted dose, the carbon K-edge remains spectrally resolved, while it has clearly evolved. The pre-peak sharpens and its intensity raises while the main peak intensity diminishes with the accumulated dose, consequently, the π* over σ* intensity ratio (see inset in Fig. 3a) increases for accumulated doses, likely related to a higher contribution of the π states to the overall signal intensity. Based on these observations, Fig. 3c displays two possible scission pathways from the acrylic resin, A and B. The scission route A involves the breakage of the carboxylic C—O bond, resulting in the formation of RO· and acyl radicals. Alternatively, route B considers the removal of the carboxilyc radical, and the byside formation of carbon radicals. It must be noted that the electron delocalization of radical especies may enhance the contribution of C π states, associated to the pre-peak intensity of the carbon K-edge [61]. Moreover, radical recombination may lead to the formation of additional π bonds. This scenario explains the increasing π over σ intensity ratio measured (see inset in Fig. 3a)), involving the decreased contribution of the σ states due to the bond scission, and the simultaneaous population of π states.

In order to assess the spectral evolution with the accumulated dose we perform a multiple linear least square (MLLS) fitting of the signal vs the accumulated dose. Reference spectra characteristic of the (almost) pristine material and of the material highly damaged (Fig. 4a) are extracted from the time series data set, being the former and last

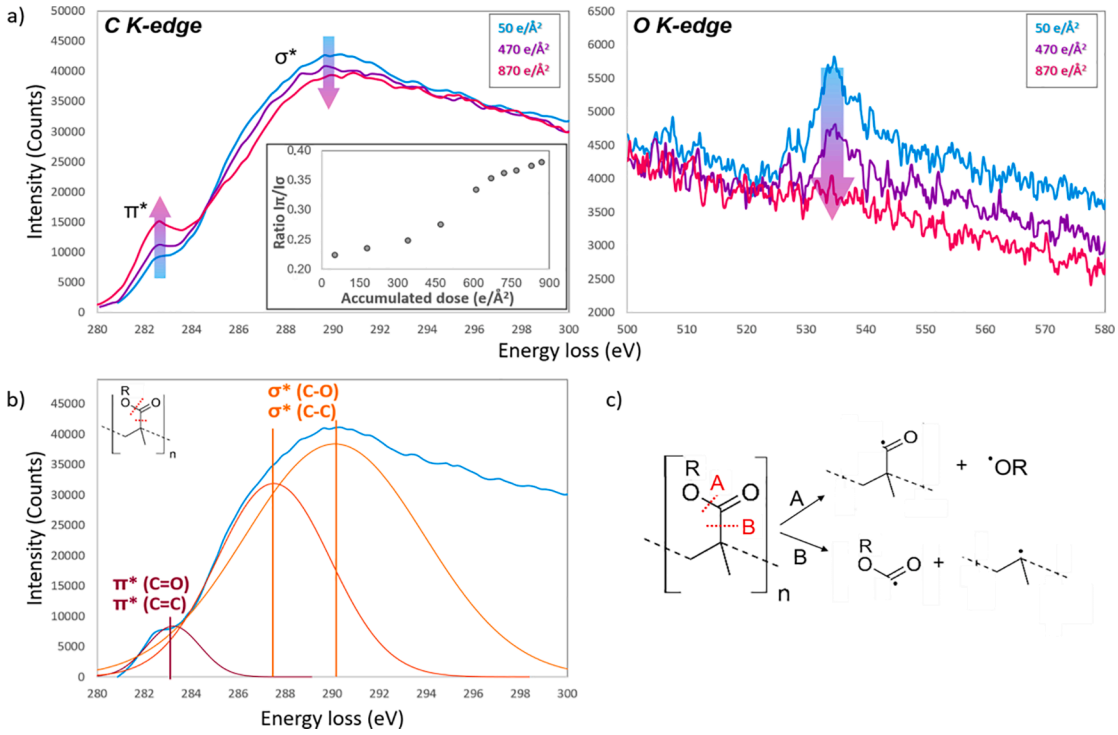

Fig. 3. (a) EELS C K-edge (left) and O K-edge (right) for increasing accumulated doses (50, 470 and 870 e/Å^2). The inset displays the intensity ratio C π*/ C σ* against the accumulated dose; (b) C K-edge gaussian decomposition into π* C═C, π* COO, σ* C—C and σ* CO contributions (spectrum taken at 50 e/Å^2); (c) Likely scission pathways of the acrylic resin during EELS experiments.

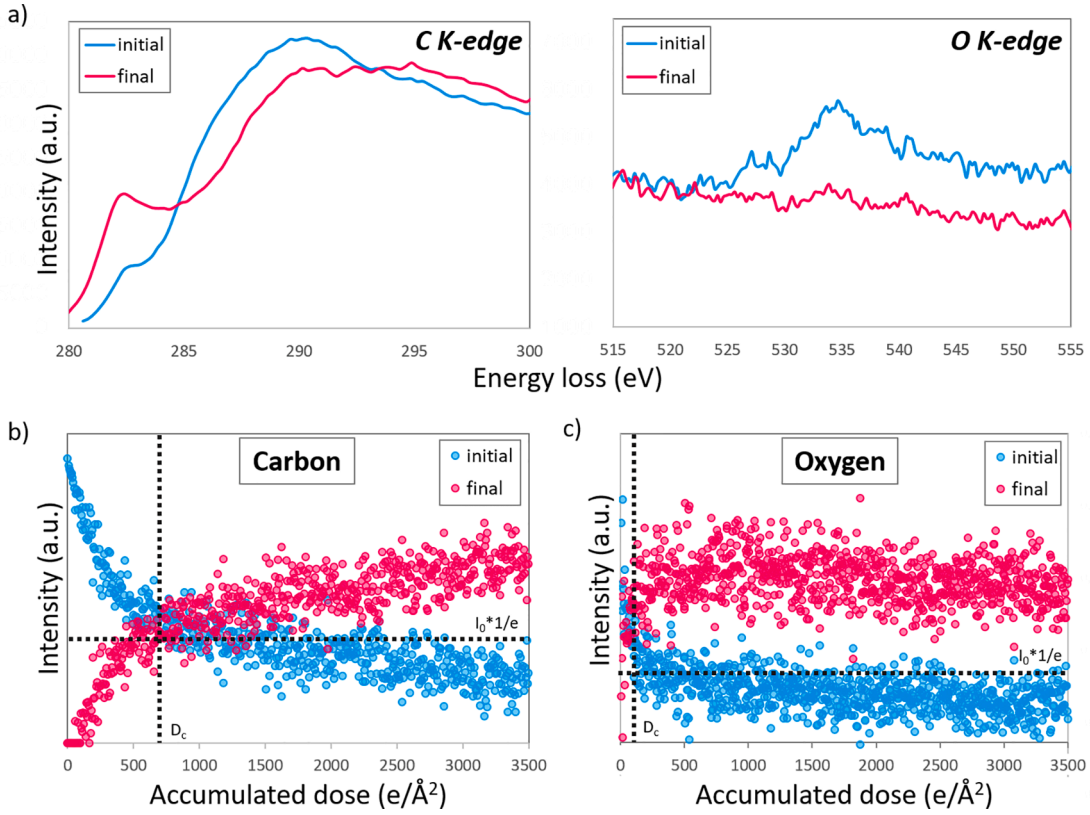

Fig. 4. (a) Pristine (blue) and highly damaged (magenta) acrylic resin reference spectra for the MLLS fit, extracted from the EELS time-series stack corresponding to the first (initial, blue) and last (final, magenta) spectra before breakage, respectively. MLLS fitting coeficients to the initial (pristine resin, blue) and final (damaged resin, magenta) reference signals, for the (b) C and (c) O K edges.

acquired spectrum, respectively. The carbon K-edge (energies between 280 and 305 eV) and oxygen K-edge (520–560 eV) signals are computed independently.

The fitting describes every spectrum as the linear combination of the established references (i.e., the pristine, *initial*, and highly damaged, *final*, acrylic resin), tracking the evolution of carbon and oxygen spectral changes as a function of the accumulated dose (Fig. 4b and c). Fig. 4b and c show the fast decrease on the signal related to the undamaged material (referred to as *initial*) with increasing accumulated dose, typically observed in many polymers and soft materials [29,62,63]. The oxygen signal (decreased/increased contribution of the initial/final reference signal) changes faster than the carbon, reaching its critical value (i.e., falling of the initial oxygen reference by a factor *e*) at accumulated doses lower than 10^2 e/Å^2 (compared to ~$7{\cdot}10^2$ e/Å^2 for the carbon). Fig. 2b shows the strong contribution of the damage reference to the spectra from 10^2 e/Å^2 accumulated doses, likely due to radiolytic decomposition, as dicussed earlier. The simultaneous carbon loss during the initial seconds of exposure to the electron beam (and, consequently, at low accumulated doses), would be also related to the radiolytic scission and cross-linking of the resin during electron irradiation. As shown in Fig. 3c, the pristine acrylic resin mainly contains carbon σ bonds, related to the main peak of the K-edge, whose scission may lead to the formation of radicals along with possible cross-linking and π bonds formation, associated to the edge pre-peak. Within this context, Drevelle et al. [64] have reported the degradation of carboxylic groups in organic phases as the starting point of resin degradation, linked to the formation of C═C and C═N bonds. Chen et al. [65] have also reported the formation of radicals and C═C bonds, along with the emission of methyl formate, methane, methanol, CO and CO_2, and further cross-linking process for higher doses on acrylic resins. In our case, the fast oxygen signal decrease, reaching the critical dose after less than 5 s (i.e., accumulated dose of $2{\cdot}10^2 \pm 5{\cdot}10^1$ e/Å^2; see Fig. 4c), might be related to the ease removal of carboxylic groups, CO and CO_2, following scission routes such as A and B (see Fig. 3c), also related to the initial decrease of the carbon intensity.

The critical doses given in Fig. 4b and c were calculated as 1/e of the estimated contribution of the *initial* signal to the spectra (MLLS fitting results) for both, carbon and oxygen, resulting in $10^3 \pm 6{\cdot}10^2$ e/Å^2 and $2{\cdot}10^2 \pm 5{\cdot}10^1$ e/Å^2, respectively. These results are in good agreement with our previous observations on the chemical evolution of the resin upon accumulated electron doses and allow depicting plausible chemical schemes inducing the acrylic resin degradation, summarized in Fig. 5.

In summary, the degradation process follows a two-fold mechanism with an accumulated dose threshold around 10^2 e/Å^2 (for 50 nm acrylic resin specimens at the used STEM-EELS experimental conditions, see

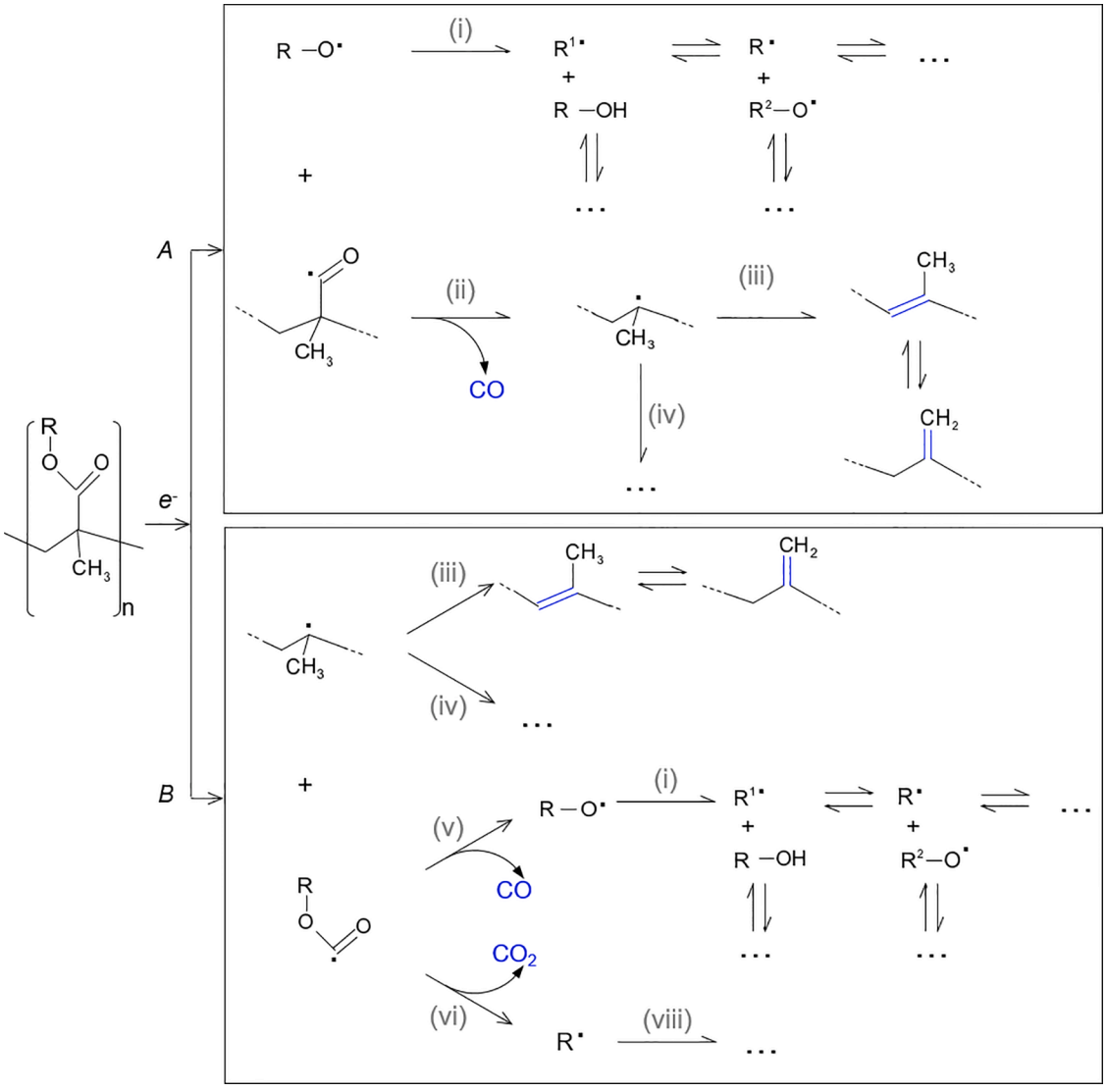

Fig. 5. Proposed chemical schemes of the reactions taking place during the degradation mechanism of acrylic resins upon accumulated electron doses.

Methods). For lower doses, the degradation is mostly dominated by radiolysis, inducing a 50% thickness reduction, which can be explained attending to the removal of carboxyl groups beside the formation of radicals (see Fig. 3c). For higher accumulated doses, the main damage process is knock-on displacement, where the radicals already created recombine and give rise to new π bonds. At doses higher than $2{\cdot}10^2$ e/Å^2 (calculated D_c for the oxygen loss) most of the oxygen has been sputtered away, while the scission of carbon σ bonds continues up to 10^3 e/Å^2 along with the aforementioned π bonds formation. Once reached 10^3 e/Å^2, (D_c related to thining and carbon edge modification) the material become prone to breakage.

The proposed degradation mechanism for thin acrylic resin specimens under the STEM conditions contributes to the knowledge on the intrincated response of sensitive materials to the electron beam, while pushes the implementation of STEM-EELS analyses and other TEM related techniques applied to such soft materials.

4. Conclusions

We investigate the damage induced in an acrylic resin for SLA during STEM-EELS experiments. We evidence the better performance of UM among several STEM specimen preparation approaches, leading to homogeneous sections with a great control on the desired thickness over wide areas ($(10^4)_n$ μm^2). Additionally, we consider different strategies to minimize electrostatic charging, to conclude that the slight benefit offered by carbon coating in reducing discharging effects may also interfere with the measured signal. By combining low-loss and core-loss EELS, we study the degradation mechanisms of acrylic resins upon electron irradiation during the measurements, demonstrating mass loss along with compositional changes while irradiating the sample. The addressed mass loss as function of the accumulated dose follows two diferentiated regimes. At low accumulated doses, the material is exponentially sputtered away, indicative of radiolytic decomposition, until thinning approximately 50% as consequence of carbon and oxygen losing at different rates. At high accumulated doses, there is a linear dependence on the mass loss with the accumulated electron dose, in agreement with knock-on damage processes. Therefore, the acrylic resin under STEM-EELS conditons is likely degraded by the sequential effect of radiolysis damage followed by knock on damage for higher accumulated doses. Moreover, monitoring the spectral shape evolution of carbon and oxygen K-edges upon increasing accumulated doses, we establish likely decomposition pathways for the acrylic resin (i.e., acyl and carbolylic radical formation turning into CO and CO_2 removal).

CRediT authorship contribution statement

L.M. Valencia: Conceptualization, Data curation, Formal analysis, Investigation, Methodology, Software, Writing – original draft. **M. de la Mata:** Conceptualization, Data curation, Formal analysis, Funding acquisition, Investigation, Methodology, Software, Supervision, Validation, Writing – original draft. **M. Herrera:** Conceptualization, Data curation, Formal analysis, Supervision, Validation, Writing – review & editing. **F.J. Delgado:** Methodology, Writing – review & editing. **J. Hernández-Saz:** Methodology, Writing – review & editing. **S.I. Molina:** Conceptualization, Funding acquisition, Validation, Writing – review & editing.

Declaration of Competing Interest

The authors declare that they have no known competing financial interests or personal relationships that could have appeared to influence the work reported in this paper.

Acknowledgments

This work has been co-financed by the 2014-2020 ERDF Operational Programme and by the Department of Economy, Knowledge, Business and University of the Regional Government of Andalucía (Ref: FEDER-UCA18-106586). Co-funding from UE and Junta de Andalucía (research group INNANOMAT, Ref. TEP946) are also acknowledged. TEM/STEM measurements were carried out at the DME-SC-ICyT-ELECMI-UCA. L. M. Valencia thanks FPI UCA Program.

Supplementary materials

Supplementary material associated with this article can be found, in the online version, at doi:10.1016/j.polymdegradstab.2022.110044.

References

[1] S.J. Pennycook, P.D. Nellist, Scanning Transmission Electron Microscopy: Imaging and Analysis, Springer New York, NY, USA, 2011. ISBN 9781441971999.
[2] D.B. Williams, C.B. Carter, Transmission Electron Microscopy: A Textbook for Materials Science, Springer New York, NY, USA, 2009. ISBN 9780387765006.
[3] N. Erdman, D.C. Bell, R. Reichelt. Scanning electron microscopy, Springer, Cham, 2019. ISBN 9783030000691.
[4] M. de la Mata, S.I. Molina, STEM tools for semiconductor characterization: beyond high-resolution imaging, Nanomaterials 12 (2022), https://doi.org/10.3390/nano12030337.
[5] G.H. Michler, W. Lebek, Electron microscopy of polymers, Springer Berlin, Heidelberg, 2008. ISBN 9783540363507.
[6] L. Du, A. Guo, A. Cai, Polydopamine-functionalised graphene–Fe_3O_4–Ag magnetic composites with high catalytic activity and antibacterial capability, Micro Nano Lett. 13 (2018) 518–523, https://doi.org/10.1049/mnl.2017.0593.
[7] M. Ohwada, Y. Mizukoshi, T. Shimokawa, N. Hayashi, Y. Hayasaka, T.J. Konno, Atomic and nanoscale imaging of a cellulose nanofiber and Pd nanoparticles composite using lower-voltage high-resolution TEM, Microscopy 66 (2017) 348–355, https://doi.org/10.1093/jmicro/dfx021.
[8] M. Kunz, K. Shull, Improved technique for cross-sectional imaging of thin polymer films by transmission electron microscopy, Polym. Commun. 34 (1993) 2427–2430.
[9] H. Hassander, Electron microscopy methods for studying polymer blends-comparison of scanning electron microscopy and transmission electron microscopy, Polym. Test. 5 (1985) 27–36, https://doi.org/10.1016/0142-9418(85)90029-7.
[10] M.R. Libera, R.A.Y.F. Egerton, Advances in the transmission electron microscopy of polymers, Polym. Rev. 50 (2010) 321–339, https://doi.org/10.1080/15583724.2010.493256.
[11] X. Mu, A. Mazilkin, C. Sprau, A. Colsmann, C. Kübel, Mapping structure and morphology of amorphous organic thin films by 4D-STEM pair distribution function analysis, Microscopy 68 (2019) 301–309, https://doi.org/10.1093/jmicro/dfz015.
[12] C. Colliex, Electron Energy Loss Spectroscopy in the Electron Microscope, 211, Elsevier Inc., 2019.
[13] J.A. Hachtel, A.R. Lupini, J.C. Idrobo, Exploring the capabilities of monochromated electron energy loss spectroscopy in the infrared regime, Sci. Rep. 8 (2018) 1–10, https://doi.org/10.1038/s41598-018-23805-5.
[14] R.F. Egerton, Electron Energy-Loss Spectroscopy in the Electron Microscope, 3rd ed., Springer, New York, 2011. EdISBN 9781441995827.
[15] R. Pal, A.K. Sikder, K. Saito, A.M. Funston, J.R. Bellare, Electron energy loss spectroscopy for polymers : a review, Polym. Chem. 8 (2017) 6927–6937, https://doi.org/10.1039/c7py01459g.
[16] R. Pal, L. Bourgeois, M. Weyland, A.K. Sikder, K. Saito, A.M. Funston, J.R. Bellare, Chemical fingerprinting of polymers using electron energy-loss spectroscopy, ACS Omega 6 (2021) 23934–23942, https://doi.org/10.1021/acsomega.1c02939.
[17] I. Gibson, D.W. Rosen, B. Stucker, Rapid Prototyping to Direct Digital Manufacturing, Springer Boston, MA, USA, 2015. ISBN 9781441911193.
[18] Q. Wu, M. Li, Y. Gu, Y. Li, Z. Zhang, Nano-analysis on the structure and chemical composition of the interphase region in carbon fiber composite, Compos. Part A Appl. Sci. Manuf. 56 (2014) 143–149, https://doi.org/10.1016/j.compositesa.2013.10.003.
[19] Y. Liu, A.L. Hamon, P. Haghi-Ashtiani, T. Reiss, B. Fan, D. He, J. Bai, Quantitative study of interface/interphase in epoxy/graphene-based nanocomposites by combining STEM and EELS, ACS Appl. Mater. Interfaces 8 (2016) 34151–34158, https://doi.org/10.1021/acsami.6b12915.
[20] L.F. Drummy, R.J. Davis, D.L. Moore, M. Durstock, R.A. Vaia, J.W.P. Hsu, Molecular-scale and nanoscale morphology of P3HT:PCBM bulk heterojunctions: energy-filtered TEM and low-dose HREM, Chem. Mater. 23 (2011) 907–912, https://doi.org/10.1021/cm102463t.
[21] S. Yakovlev, K.H. Downing, Visualization of clusters in polymer electrolyte membranes by electron microscopy, Phys. Chem. Chem. Phys. 15 (2013) 1052–1064, https://doi.org/10.1039/c2cp42969a.
[22] C. Wang, G. Duscher, S.J. Paddison, Electron energy loss spectroscopy of polytetrafluoroethylene: experiment and first principles calculations, Microscopy 63 (2014) 73–83, https://doi.org/10.1093/jmicro/dft046.
[23] K. Varlot, J.M. Martin, C. Quet, EELS analysis of PMMA at high spatial resolution, Micron 32 (2001) 371–378, https://doi.org/10.1016/S0968-4328(00)00017-2.

[24] R.F. Egerton, S. Lazar, M. Libera, Delocalized radiation damage in polymers, Micron 43 (2012) 2–7, https://doi.org/10.1016/j.micron.2011.05.007.
[25] J. Ayache, L. Beaunier, J. Boumendil, G. Ehret, D. Laub, Sample Preparation Handbook for Transmission Electron Microscopy, Springer New York, NY, USA, 2010. ISBN 9781441959751.
[26] P.R. Munroe, The application of focused ion beam microscopy in the material sciences, Mater. Charact. 60 (2009) 2–13, https://doi.org/10.1016/j.matchar.2008.11.014.
[27] M.L. Ericson, H. Lindberg, Design and potential of instrumented ultramicrotomy, Polymer 38 (1997) 4485–4489, https://doi.org/10.1016/S0032-3861(96)01051-8 (Guildf).
[28] T.R. Matzelle, H. Gnaegi, A. Ricker, R. Reichelt, Characterization of the cutting edge of glass and diamond knives for ultramicrotomy by scanning force microscopy using cantilevers with a defined tip geometry. Part II, J. Microsc. 209 (2003) 113–117, https://doi.org/10.1046/j.1365-2818.2003.01119.x.
[29] R.F. Egerton, P. Li, M. Malac, Radiation damage in the TEM and, SEM 35 (2004) 399–409, https://doi.org/10.1016/j.micron.2004.02.003.
[30] R. Egerton, Radiation damage and nanofabrication in TEM and STEM, Microsc. Today 29 (2021) 56–59, https://doi.org/10.1017/s1551929521000663.
[31] D.T. Grubb, Radiation damage and electron microscopy of organic polymers, J. Mater. Sci. 9 (1974) 1715–1736, https://doi.org/10.1007/BF00540772.
[32] R.F. Egerton, Radiation damage to organic and inorganic specimens in the TEM, Micron 119 (2019) 72–87, https://doi.org/10.1016/j.micron.2019.01.005.
[33] J. Cazaux, Correlations between ionization radiation damage and charging effects in transmission electron microscopy, Ultramicroscopy 60 (1995) 411–425, https://doi.org/10.1016/0304-3991(95)00077-1.
[34] C. Guo, F.I. Allen, Y. Lee, T.P. Le, C. Song, J. Ciston, A.M. Minor, E.D. Gomez, Probing local electronic transitions in organic semiconductors through energy-loss spectrum imaging in the transmission electron microscope, Adv. Funct. Mater. 25 (2015) 6071–6076, https://doi.org/10.1002/adfm.201502090.
[35] Z.J.W.A. Leijten, A.D.A. Keizer, G. De With, H. Friedrich, Quantitative analysis of electron beam damage in organic thin films, J. Phys. Chem. C 121 (2017) 10552–10561, https://doi.org/10.1021/acs.jpcc.7b01749.
[36] O. Cretu, Y.C. Lin, K. Suenaga, Inelastic electron irradiation damage in hexagonal boron nitride, Micron 72 (2015) 21–27, https://doi.org/10.1016/j.micron.2015.02.002.
[37] R.F. Egerton, Control of radiation damage in the TEM, Ultramicroscopy 127 (2013) 100–108, https://doi.org/10.1016/j.ultramic.2012.07.006.
[38] Z.J.W.A. Leijten, M.J.M. Wirix, M. Strauss, J.M. Plitzko, G. de With, H. Friedrich, Low-dose (S)TEM elemental analysis of water and oxygen uptake in beam sensitive materials, Ultramicroscopy 208 (2020), https://doi.org/10.1016/j.ultramic.2019.112855.
[39] O. Dyck, S. Hu, S. Das, J. Keum, K. Xiao, B. Khomami, G. Duscher, Quantitative phase fraction detection in organic photovoltaic materials through EELS imaging, Polymers 7 (2015) 2446–2460, https://doi.org/10.3390/polym7111523 (Basel).
[40] B. Kuei, E.D. Gomez, Elucidating mechanisms for electron beam damage in conjugated polymers, Microsc. Microanal. 24 (2018) 1988–1989, https://doi.org/10.1017/s1431927618010425.
[41] Y. Liu, A.L. Hamon, B. Fan, D. He, P. Haghi-Ashtiani, T. Reiss, J. Bai, Intensive EELS study of epoxy composites reinforced by graphene-based nanofillers, J. Appl. Polym. Sci. 135 (2018) 1–8, https://doi.org/10.1002/app.46748.
[42] D.T. Grubb, G.W. Groves, Rate of damage of polymer crystals in the electron microscope: dependence on temperature and beam voltage, Philos. Mag. 24 (1971) 815–828, https://doi.org/10.1080/14786437108217051.
[43] L.G. Lis, A.P. Hitchcock, V. Berejnov, D. Susac, J. Stumper, G.A. Botton, Evaluating focused ion beam and ultramicrotome sample preparation for analytical microscopies of the cathode layer of a polymer electrolyte membrane fuel cell, J. Power Sources 312 (2016) 23–35, https://doi.org/10.1016/j.jpowsour.2016.02.019.
[44] P.K. Singh, B.R. Venugopal, D.R. Nandini, Effect of electron beam irradiation on polymers, J. Mod. Mater. 5 (2018) 24–33, https://doi.org/10.1063/1.4710140.
[45] K. Iakoubovskii, K. Mitsuishi, Y. Nakayama, K. Furuya, Thickness measurements with electron energy loss spectroscopy, Microsc. Res. Tech. 71 (2008) 626–631, https://doi.org/10.1002/jemt.20597.
[46] H. Zhang, R. Egerton, M. Malac, EELS investigation of the formulas for inelastic mean free path, Microsc. Microanal. 17 (2011) 1466–1467, https://doi.org/10.1017/s1431927611008208.
[47] C.J. Russo, L.A. Passmore, Ultrastable gold substrates: properties of a support for high-resolution electron cryomicroscopy of biological specimens, J. Struct. Biol. 193 (2016) 33–44, https://doi.org/10.1016/j.jsb.2015.11.006.
[48] R.M. Glaeser, K.H. Downing, Specimen charging on thin films with one conducting layer : discussion of physical principles, Microsc. Microanal. 10 (2004) 790–796.
[49] C.J. Russo, L.A. Passmore, Controlling protein adsorption on graphene for cryo-EM using low-energy hydrogen plasmas, Nat. Methods 11 (2014) 773, https://doi.org/10.1038/nmeth0714-773e.
[50] K. Sader, M. Stopps, L.J. Calder, P.B. Rosenthal, Cryomicroscopy of radiation sensitive specimens on unmodified graphene sheets: reduction of electron-optical effects of charging, J. Struct. Biol. 183 (2013) 531–536, https://doi.org/10.1016/j.jsb.2013.04.014.
[51] B. Singh, N. Sharma, Mechanistic implications of plastic degradation, Polym. Degrad. Stab. 93 (2008) 561–584, https://doi.org/10.1016/j.polymdegradstab.2007.11.008.
[52] T. Susi, J.C. Meyer, J. Kotakoski, Quantifying transmission electron microscopy irradiation effects using two-dimensional materials, Nat. Rev. Phys. 1 (2019) 397–405, https://doi.org/10.1038/s42254-019-0058-y.
[53] J.R. Fryer, Radiation damage in organic crystalline films, Ultramicroscopy 14 (1984) 227–236, https://doi.org/10.1016/0304-3991(84)90091-3.
[54] K. Siangchaew, M. Libera, The influence of fast secondary electrons on the aromatic structure of polystyrene, Philos. Mag. A Phys. Condens. Matter Struct. Defects Mech. Prop. 80 (2000) 1001–1016, https://doi.org/10.1080/01418610008212095.
[55] B. Kuei, E.D. Gomez, Pushing the limits of high-resolution polymer microscopy using antioxidants, Nat. Commun. (2021) 12, https://doi.org/10.1038/s41467-020-20363-1.
[56] M.B. Braunfeld, A.J. Koster, J.W. Sedat, D.A. Agard, Cryo automated electron tomography: towards high-resolution reconstructions of plastic-embedded structures, J. Microsc. 174 (1994) 75–84, https://doi.org/10.1111/j.1365-2818.1994.tb03451.x.
[57] R.F. Egerton, Mechanisms of radiation damage in beam-sensitive specimens, for TEM accelerating voltages between 10 and 300 kV, Microsc. Res. Tech. 75 (2012) 1550–1556, https://doi.org/10.1002/jemt.22099.
[58] O. Ugurlu, J. Haus, A.A. Gunawan, M.G. Thomas, S. Maheshwari, M. Tsapatsis, K. A. Mkhoyan, Radiolysis to knock-on damage transition in zeolites under electron beam irradiation, Phys. Rev. B Condens. Matter Mater. Phys. 83 (2011) 1–4, https://doi.org/10.1103/PhysRevB.83.113408.
[59] K. Varlot, J.M. Martin, D. Gonbeau, C. Quet, Chemical bonding analysis of electron-sensitive polymers by EELS, Polymer 40 (1999) 5691–5697, https://doi.org/10.1016/S0032-3861(98)00782-4 (Guildf).
[60] K. Varlot, J.M. Martin, C. Quet, Y. Kihn, Towards sub-nanometer scale EELS analysis of polymers in the TEM, Ultramicroscopy 68 (1997) 123–133, https://doi.org/10.1016/S0304-3991(97)00019-3.
[61] K. Varlot, J.M. Martin, C. Quet, Physical and chemical changes in polystyrene during electron irradiation using EELS in the TEM: contribution of the dielectric function, J. Microsc. 191 (1998) 187–194, https://doi.org/10.1046/j.1365-2818.1998.00376.x.
[62] S. Yakovlev, M. Misra, S. Shi, E. Firlar, M. Libera, Quantitative nanoscale water mapping in frozen-hydrated skin by low-loss electron energy-loss spectroscopy, Ultramicroscopy 110 (2010) 866–876, https://doi.org/10.1016/j.ultramic.2010.03.014.
[63] R.F. Egerton, I. Rauf, Dose-rate dependence of electron-induced mass loss from organic specimens, Ultramicroscopy 80 (1999) 247–254, https://doi.org/10.1016/S0304-3991(99)00114-X.
[64] C. Drevelle, S. Duquesne, M. Le Bras, J. Lefebvre, R. Delobel, A. Castrovinci, C. Magniez, M. Vouters, Influence of ammonium polyphosphate on the mechanism of thermal degradation of an acrylic binder resin, J. Appl. Polym. Sci. 94 (2004) 717–729, https://doi.org/10.1002/app.20868.
[65] J.K. Chen, F.H. Ko, F.C. Chang, Structural transformation of acrylic resin upon controlled electron-beam exposure yields positive and negative resists, Adv. Funct. Mater. 15 (2005) 1147–1154, https://doi.org/10.1002/adfm.200400077.